

Visualizing Diffusion Tensor MR Images Using Streamtubes and Streamsurfaces

Song Zhang, Çagatay Demiralp, and David H. Laidlaw

Abstract—We present a new method for visualizing 3D volumetric diffusion tensor MR images. We distinguish between linear anisotropy and planar anisotropy and represent values in the two regimes using streamtubes and streamsurfaces, respectively. Streamtubes represent structures with primarily linear diffusion, typically fiber tracts; streamtube direction correlates with tract orientation. The cross-sectional shape and color of each streamtube represent additional information from the diffusion tensor at each point. Streamsurfaces represent structures in which diffusion is primarily planar. Our algorithm chooses a very small representative subset of the streamtubes and streamsurfaces for display. We describe the set of metrics used for the culling process, which reduces visual clutter and improves interactivity. We also generate anatomical landmarks to identify the locations of such structures as the eyes, skull surface, and ventricles. The final models are complex surface geometries that can be imported into many interactive graphics software environments. We describe a virtual environment to interact with these models. Expert feedback from doctors studying changes in white-matter structures after gamma-knife capsulotomy and preoperative planning for brain tumor surgery shows that streamtubes correlate well with major neural structures, the 2D section and geometric landmarks are important in understanding the visualization, and the stereo and interactivity from the virtual environment aid in understanding the complex geometric models.

Index Terms—Diffusion tensor imaging, DT-MRI, DTI, hyperstreamline, immersive virtual reality, streamsurface, streamtube, scientific visualization, volume visualization.



1 INTRODUCTION

DIFFUSION tensor MR imaging (DT-MRI) of *in vivo* biological tissues produces a 3D second-order tensor field [1] describing the diffusion rate at every sample point in a 3D volume. Water diffusion in tissue due to Brownian motion is random, but the tissue microstructures restrict it. In white matter, water motion perpendicular to axons is restricted by the tightly packed multiple myelin membranes encompassing them [21]. This anisotropy is evident in the MR measurements, which can be used noninvasively to explore the white matter structures *in vivo*. Although a single axon can be as thin as a few microns, many neural fiber tracts are coherent bundles that are well above the voxel size of the DT-MRI data. Diffusion anisotropy has been linked to the highly structured nerve fibers in brain white matter [14], [10]. Several groups have confirmed that, in the heart, the normalized major eigenvector of the diffusion tensor lies parallel to the local fiber tract direction [7], [9]. Here, we use the terms *major* eigenvector, *medium* eigenvector, and *minor* eigenvector, or the symbols e_1 , e_2 , and e_3 , for the three eigenvectors of the diffusion tensor matrix ordered by decreasing eigenvalue. High-angular-resolution diffusion measurements have also been explored to characterize diverse fiber structure within a single voxel [13].

Visualizing a 3D diffusion tensor field is difficult because of the large amount of information it contains. Each sample point in the data set consists of a second-order tensor,

represented by a 3×3 symmetric matrix, so that there are six interrelated quantities at each sample point. Visualizing these six variables separately does not show the relationships among them; however, visualizing them all simultaneously in one image is rarely possible. While complete visualization of diffusion tensor fields has been described for two-dimensional data sets [12], [16], these methods suffer from various limitations when extended to 3D, as discussed in the next section.

Our goal, however, is to illustrate certain structures in biological tissues; visualizing all the information is often unnecessary for this purpose. Instead, we choose to visualize only the information that reveals connectivity or other microstructural details within the tissue.

Our approach distinguishes between linear and planar structures and uses what we call streamtubes and streamsurfaces to visualize these types of structures. Streamtubes represent linear diffusion, which tends to be produced by fibrous structures. The cross-section and color of each streamtube represent the additional components of the diffusion measurements along the trajectories of fiber tracts. Streamsurfaces represent structures in which diffusion is primarily planar. We first generate a large number of streamtubes and streamsurfaces covering all the regions of interest, then use a culling algorithm to remove most of them while retaining a representative set. To provide a context for the streamtubes and streamsurfaces, we also display anatomical landmarks such as the eyes, skull surface, and ventricles. Fig. 1 shows a visualization of a human brain data set created using our method.

The conventional desktop display limits our ability to understand complex geometric models. We have developed a virtual environment that displays these models and allows users to interact with them.

• The authors are with the Department of Computer Science, Brown University, Providence, RI 02912.
E-mail: {sz, cad, dhl}@cs.brown.edu.

Manuscript received 22 Jan. 2002; revised 15 Sept. 2002; accepted 16 Oct. 2002.

For information on obtaining reprints of this article, please send e-mail to: tcg@computer.org, and reference IEEECS Log Number 115742.

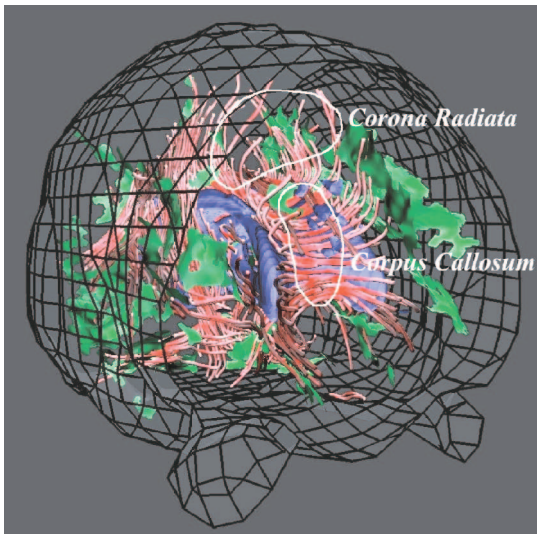


Fig. 1. Visualization of a human brain using our method. Geometric models include the red streamtubes, the green streamsurfaces, the blue ventricle surface, and the wireframe skull surface. Large neural structures such as the corpus callosum and the corona radiata are represented by the red streamtubes in this view.

2 RELATED WORK

Researchers have designed visualization methods that represent completely a 2D slice of a 3D diffusion tensor field. Several attempts to visualize 3D DT-MRI data have also been made recently. Pierpaoli and Basser. use arrays of ellipsoids to represent a two-dimensional diffusion tensor field [16]. Since the diffusion tensor matrix is symmetric and has positive eigenvalues, an ellipsoid is its natural geometric representation. Each axis of the ellipsoid represents one eigenvector and its corresponding eigenvalue. Laidlaw et al. normalize the sizes of the ellipsoids to give a more continuous appearance and, in a second method, borrow concepts from oil painting to display diffusion tensor images [12]. Two-dimensional brush strokes built up in several layers represent different features of the diffusion tensors.

The two-dimensional methods in [16] and [12] visualize a diffusion tensor field by completely visualizing the tensors of discrete sample points. When applied to a 3D data set, such methods have two limitations:

- Visualizing every sample point in the 3D data set produces so many ellipsoids or brushstrokes that internal structures are difficult to see.
- The continuity inherent in biological tissues is not properly represented in the final image. For example, neural fibers in the brain are difficult to locate within an array of ellipsoids.

Several methods for 3D diffusion tensor field visualization have been developed to address these problems, each making different choices about the subset of the tensor information to represent and how to represent it.

Dickinson, in his design of visualization software for tensor field data sets, tracks tensor field lines that are everywhere parallel to an eigenvector of a 3D tensor field [18]. The present work uses this same construction. Delmarcelle and Hesselink built on this in proposing hyperstreamlines, visual icons for representing tensor

information along a trajectory [6]. The idea behind this method, which is analogous to using an ellipsoid to represent one diffusion tensor, is to visualize *all* the information but only at *some* locations. The trajectory of the hyperstreamline is generated from the vector field defined by the major eigenvector of the tensor. The cross-sectional shape and color along the trajectory encode information about the other two eigenvectors and the magnitude of the major eigenvector. The hyperstreamline method has been applied to both stress tensor fields and momentum flux density tensor fields but not to diffusion tensor fields.

Xue et al. track streamlines in the major eigenvector field of the diffusion tensor field to visualize DT-MRI data sets [23]. For DT-MRI data sets, the major eigenvector of the tensor matrix is in the direction of fastest diffusion. Xue et al. use a fiber-tracking method dubbed FACT [15] to track the linear features in biological tissues following the major eigenvector of each diffusion tensor. There are other methods for tracking linear features in diffusion tensor data sets: Weinstein et al. stabilize the tracking in regions with nonlinear preferential diffusion using their tensorlines method [20] and Basser et al. use numerical methods to solve a Frenet equation describing the evolution of a fiber tract [2]. These methods are, however, constrained to visualizing only one vector field and neither paper discusses the sampling and placement of the tracts in the image.

Kindlmann and Weinstein take a volume-rendering approach to the problem [11]. Their method displays only some of the information, but displays that information densely within a volume. A hue-ball and a barycentric map assign color and opacity to each point based on the diffusion measurements. The result shows the data set at high resolution. However, the composition into a single pixel of many data points along a ray makes it difficult to discern any given point, and the paths of fibrous structures are hard to see.

Our goal is to visualize connectivity and tissue microstructure in MR diffusion tensor images of biological tissue. The streamtubes we use here build on hyperstreamlines but attempt to overcome their limitations in this context:

- The cross-section of a hyperstreamline can grow quite large, limiting the density of hyperstreamlines in a scene and, thus, the level of detail we can visualize.
- The images in hyperstreamline papers generally contain only a few hyperstreamlines. To visualize microstructures in biological tissues, we need more hyperstreamlines in the scene.
- While a hyperstreamline is an intuitive visual representation for linear structures in biological tissue, it is not very effective for representing planar diffusion.

3 OUR APPROACH

We distinguish between regions of linear and planar anisotropy and employ streamtubes and streamsurfaces, respectively, to visualize these two types of regions [25]. Section 4.1 describes classifying different kinds of anisotropies. In Section 4.2, we discuss issues related to streamtubes,

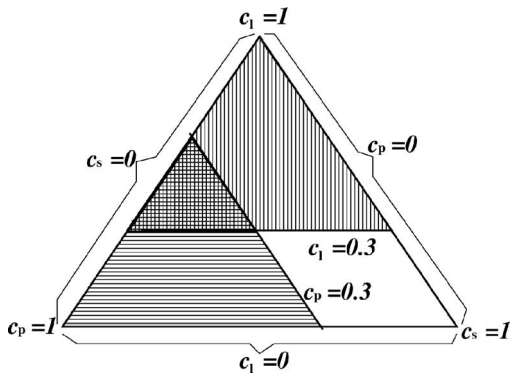


Fig. 2. Barycentric map for the definition of anisotropy regions. Here, linear anisotropy regions are defined as $c_l > 0.3$ (vertically hatched area); planar anisotropy regions are defined as $c_p > 0.3$ (horizontally hatched area). The small crosshatched triangle has both linear anisotropy and planar anisotropy by this definition.

including their definition, the extension of the trajectories they follow, how to sample the seed points for an initial trajectory set so that all the data are covered, and how to select a representative set from the whole trajectory set. Section 4.3 explains the strategies for generating streamsurfaces in regions of planar anisotropy. We also generate geometric representations of anatomical landmarks to provide context, as discussed in Section 4.4. Finally, in Section 4.5, we describe our virtual environment to display and interact with the complex geometric models [24], [26].

3.1 Anisotropy Classification

Westin et al. [22] define three characteristic qualities of a diffusion tensor value based on the three eigenvalues, $\lambda_1 \geq \lambda_2 \geq \lambda_3$:

$$c_l = \frac{\lambda_1 - \lambda_2}{\lambda_1 + \lambda_2 + \lambda_3},$$

$$c_p = \frac{2(\lambda_2 - \lambda_3)}{\lambda_1 + \lambda_2 + \lambda_3},$$

$$c_s = \frac{3\lambda_3}{\lambda_1 + \lambda_2 + \lambda_3},$$

where c_l represents linear anisotropy, c_p represents planar anisotropy, and c_s represents isotropy. Note that these values are complementary, $c_l + c_p + c_s = 1$.

A diffusion tensor with one eigenvalue much larger than the other two has large c_l , corresponding to linear anisotropy; white-matter tracts tend to produce tensors with linear anisotropy [4]. A diffusion tensor with two large and one small eigenvalue has large c_p , corresponding to planar anisotropy; sheet-like structures and crossings of fiber tracts in biological tissues are likely to yield planar anisotropy. Diffusion tensors whose three eigenvalues are roughly the same imply an underlying structure with no preferred diffusion direction; these tensors are isotropic and have a large c_s . Gray matter in the brain tends to produce isotropic diffusion tensors [1].

There are other anisotropy metrics, such as relative anisotropy (RA) or fractional anisotropy (FA) [16], that measure the variance of the eigenvalues and provide a directionless scale value. Such metrics measure differences among anisotropies, but do not distinguish between linear



Fig. 3. Streamtubes representing regions of linear anisotropy in a human brain. The long U-shaped tubes pass through the corpus callosum and project into the corona radiata.

and planar anisotropies and isotropies. Westin et al.'s metrics, on the other hand, measure these kinds of anisotropies separately.

We define linear anisotropy regions and planar anisotropy regions by setting thresholds on c_l and c_p . We can use a barycentric map [11] to look at the defined anisotropy regions (see Fig. 2). Note that this definition allows diffusion tensors to have both linear and planar anisotropy so that streamtubes and streamsurfaces can be generated in the same region. From our observations, those regions are usually where linear structures transition to planar ones, often where neural fibers fan out or near intersecting tracts.

3.2 Streamtubes for Linear Anisotropy

We chose streamtubes as the geometric primitive to represent linear anisotropy because they can naturally represent the underlying linear structures, can carry additional information provided by the diffusion tensors, and have the potential to reduce visual clutter.

The visual mapping of the streamtube is similar to that of the hyperstreamline. The trajectory sweeps along the major eigenvector field and the cross-sectional shape is an ellipse representing the ratio of the other two eigenvectors. The radius corresponding to the medium eigenvector is set to a constant to keep the streamtube slim, while the ratio between the medium and the minor eigenvectors is preserved. The color of the streamtube shows the linear anisotropy value: Greater anisotropy is redder.

The major eigenvector field is the primary information visualized by streamtubes. We first fill the regions of linear anisotropy with a dense set of streamtubes and then select a representative subset. The four steps that generate a representative set of streamtubes are: picking the seed points for a dense set of trajectories covering the regions of linear anisotropy, calculating trajectories in the major eigenvector field, selecting a sparser representative set of trajectories from the dense set, and visualizing additional information such as the direction of the medium and minor eigenvectors. Fig. 3 shows the streamtubes generated from a human brain data set.

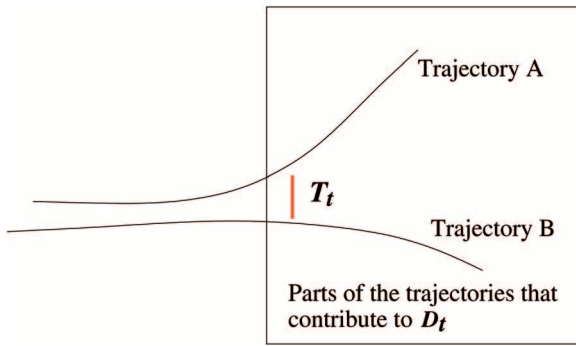


Fig. 4. In order to emphasize important differences between a pair of trajectories, we average the distance between them only over the region where they are at least T_t apart; smaller differences are assumed to be insignificant.

3.2.1 Seed Points

Streamtube seed points are chosen so that streamtubes pass through all regions of high linear anisotropy. Recall that we reduce the number of trajectories later, so it is acceptable to generate many trajectories now.

The seed points are not restricted to the sample points of the volume image. At any point within the data volume, we use tricubic B-spline functions to interpolate the tensor field [2], so there is no limit on how many seed points we use or where we put them. We generate a seed point from every sample point by jittering it within a voxel [8].

3.2.2 Trajectories

Each streamline begins from a seed point and follows the major eigenvector field both forward and backward. We find the integral curve passing through the seed point using a second-order Runge-Kutta integration method [17], [2]. (We also experimented with fourth-order Runge-Kutta, with the results very similar to those generated by the second-order method.) Because streamtubes represent regions of high linear anisotropy, their trajectories are restricted to these regions. Also, the streamtubes are clipped to the data volume and to regions of sufficiently high signal-to-noise ratio.

3.2.3 Culling

Our sampling method starts with 1.2 million seed points and produces more than 150,000 trajectories on a $256 \times 256 \times 144$ human brain data set. Visualizing all the streamtubes is not only expensive but also undesirable as including too many streamtubes in the scene would block the inner structures. A selection algorithm culls most of the trajectories and keeps only a representative set. We use three metrics for the culling process: the length of a trajectory, the average linear anisotropy along a trajectory, and the similarity between a trajectory and the group of trajectories already selected. Trajectories are kept or discarded according to their metrics. For example, a trajectory that is too similar to a selected trajectory is discarded.

We define the similarity between two trajectories using a distance measure:

TABLE 1
Parameters Used to Select Streamtubes
for Figs. 1, 3, 10, and 11

Streamtube length	> 18.0 mm
Average linear anisotropy	> 0.30
T_t used in D_t for streamtubes	0.89 mm
Distance between lines, D_t	> 4.5 mm

$$D_t = \frac{\int_{s_0}^{s_1} \max(\text{dist}(s) - T_t, 0) ds}{\int_{s_0}^{s_1} \max\left(\frac{\text{dist}(s) - T_t}{|\text{dist}(s) - T_t|}, 0\right) ds},$$

where s parameterizes the arc length of the shorter trajectory, s_0 and s_1 are the starting and end points of s , and $\text{dist}(s)$ is the shortest distance from location s on the shorter trajectory to the longer trajectory. T_t ensures that we label two trajectories as different if they differ significantly over any portion of the arc length. For example, if $T_t = 0$, the pair of trajectories shown in Fig. 4 would have a small D_t value because they run close together over much of their length, making the denominator large. Setting T_t as in Fig. 4 makes D_t larger because it reduces the denominator.

Note that we use the distance between the two trajectories as a measure of similarity. Other features such as the curvature of the trajectories can also be used to measure similarity. Since DT-MRI data are averaged over the size of the voxel, the trajectories tracked are usually smooth. Thus, the distance between the trajectories makes a decent measurement of the similarity.

For each of the three criteria, we set a threshold to limit the streamtubes we draw. Table 1 shows the thresholds for this culling process for Figs. 1, 3, 10, and 11.

3.2.4 Shape and Color

The trajectory visually represents the major eigenvector field of the diffusion tensor field. Once we have generated a representative set of streamtube trajectories, we map additional information to them and construct the streamtubes. The cross-section of a streamtube at a given point is an ellipse representing the other two eigenvectors and eigenvalues, as shown in Fig. 5. We set the radius along the

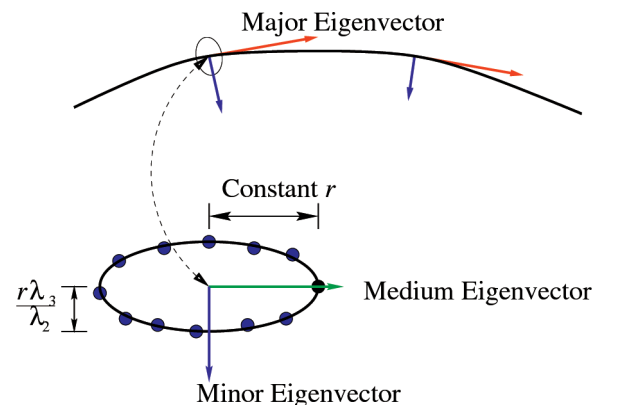


Fig. 5. Generating a streamtube from a trajectory and cross-section. The second and third eigenvalues of the diffusion tensor, λ_2 and λ_3 , define the relative shape of the cross-section. Its orientation is defined by the corresponding eigenvectors.

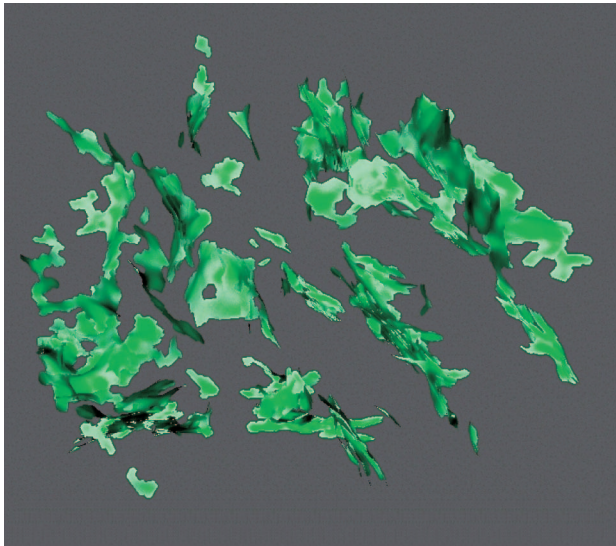


Fig. 6. Streamsurfaces extend along major and medium eigenvectors in regions of planar anisotropy.

medium eigenvector to a constant, but preserve the aspect ratio of the second and third eigenvalues. Adjacent cross-sections are connected to form the streamtube. The color of the streamtube is based on the linear anisotropy value, with saturated red for the maximum and white for the minimum.

3.3 Streamsurfaces for Planar Anisotropy

Diffusion tensors with planar anisotropy could result from a surface structure, a boundary between different materials, or a crossing of multiple linear features. Visualizing regions of planar anisotropy may help to illustrate these kinds of structures.

The streamsurface is the approximation of the surface that extends along both the major eigenvector field and medium eigenvector field. At any point on a streamsurface, the major and medium eigenvectors lie in the tangent plane to the surface. Given a starting point in the volume, we expand a streamsurface by following these two vector fields. We first generate many streamsurfaces and then select a subset of them for display. Colors are mapped to the surfaces to represent the planar anisotropy, c_s , at each point.

3.3.1 Seed Points

As for streamtubes, we generate seed points by jittering every sample point in the data set.

3.3.2 Surface Generation

The surface generation algorithm follows the planar structure suggested by the planar anisotropy. We define $T(v)$ as the diffusion tensor at point v and $P(v)$ as the plane that contains the major and medium eigenvectors of $T(v)$ as well as v . $P(v)$ is tangent to the streamsurface.

1. Starting from a seed point, v , we set the initial directions radially along six evenly distributed directions within $P(v)$ and extend curved edges to follow the shape of the surface (see Step 3). We then generate a triangle for every pair of the neighboring edges (two edges are neighbors if their projections on $P(u)$ are neighbors).

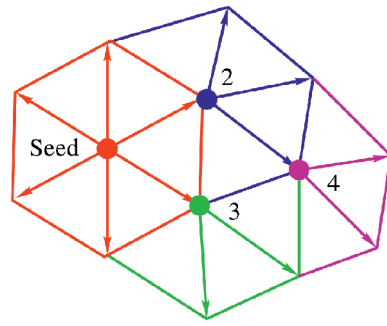


Fig. 7. Expanding a streamsurface. Begin at the point labeled Seed, add the red edges; repeat the expansion at points 2, 3, 4, etc., as many times as possible.

2. For every new vertex u extended from Step 1, we project to $P(u)$ the existing triangles that are attached to u and then extend curved edges (see Step 3) from the initial directions on $P(u)$ that are not covered by the existing triangles. Then, we generate a triangle for every pair of neighboring edges. This step is repeated for every newly generated vertex until the terminating conditions in Step 4 are met.
3. We extend the edges from a vertex u by integrating in the 2D vector field V , which is defined on the plane P_1 that is both perpendicular to $P(u)$ and contains the initial direction of extension in $P(u)$. V is defined at every point x in P_1 as the the linear combination of the normalized major and medium eigenvector of $T(x)$ that lies within P_1 . We ensure the consistency of the integration directions by swapping $V(x)$ if the dot product of $V(x)$ and the initial direction is negative. We use second-order Runge-Kutta for the integration.
4. The extension stops when it goes outside the data boundary, hits a low planar anisotropy region, enters a region of low signal-to-noise ratio, or incurs a high-curvature turn.

Fig. 7 illustrates the order of the first few extensions starting from a seed point.

3.3.3 Culling

As in streamtube selection, we use the following three criteria in surface selection: the area of the surface, the average planar anisotropy of the surface, and the distance between the surface and other selected surfaces. We eliminate a surface if it is too small, too low in average planar anisotropy, or too close to other selected surfaces.

The distance between two surfaces is defined as:

$$D_s = \frac{\iint_{\Omega} \max(\text{dist}(\omega) - T_s, 0) d\omega}{\iint_{\Omega} \max\left(\frac{\text{dist}(\omega) - T_s}{|\text{dist}(\omega) - T_s|}, 0\right) d\omega}.$$

Like the definition of distance between curves, this metric gives the average above-threshold distance between two surfaces.

Table 2 shows the thresholds for culling streamsurfaces for Figs. 1, 6, 10, and 11.

TABLE 2
Parameters Used to Select Streamsurfaces
for Figs. 1, 6, 10, and 11

Surface size	$> 7.00 \text{ mm}^2$
Average planar anisotropy	> 0.30
T_s used in D_s for streamsurfaces	1.34 mm
Distance between surfaces, D_s	$> 8.9 \text{ mm}$

3.4 Anatomical Landmarks

Feedback from preliminary results showed that biologists can explore images more effectively if they can see some familiar anatomical structures. Thus, we generate isosurfaces of a few anatomical features from T_2 -weighted images using AVS [19].

Water has a higher T_2 -weighted intensity than white and gray matter; white and gray matter, in turn, have higher T_2 -weighted intensities than air. We generate an approximate boundary between fluid and other tissue that echoes the shape of the ventricles by generating an isosurface at a level between the intensity of water and that of other tissue. While these shapes are not precise, their presence makes the images much easier to interpret. Surfaces of other anatomical structures, such as blood vessels or tumors, can also be generated for certain applications.

3.5 Virtual Reality

Compared to still pictures and desktop display, an immersive virtual environment such as the Cave [5] offers the advantages of a head-tracked stereo display, a large display surface, and interactivity. We take advantage of these features by showing our visualization in the Cave.

Our Cave, shown in Fig. 8, is an 8' cube with rear-projected front and side walls and a front-projected floor. The user wears LCD shutter glasses with an attached tracker and uses the wand, a mouse-like input device that is also tracked, to interact with the virtual world.

We put geometric models including streamtubes, streamsurfaces, and anatomical landmarks at approximately the center of the Cave and orient them so that the front of the brain always faces the opening of the Cave. We then display a 2D section that carries a slice of the

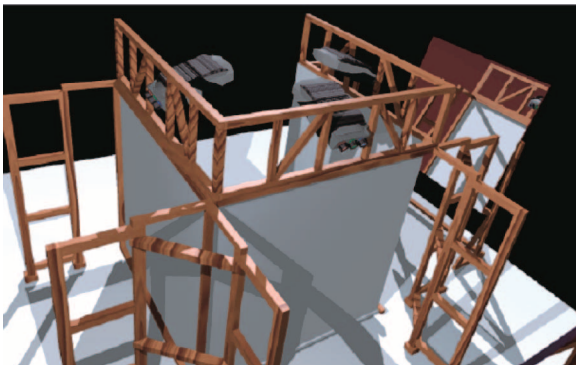


Fig. 8. A model of the Cave viewed from behind the back wall. The user stands inside the three rear-projected walls and sees a virtual world on the head-tracked stereo displays.

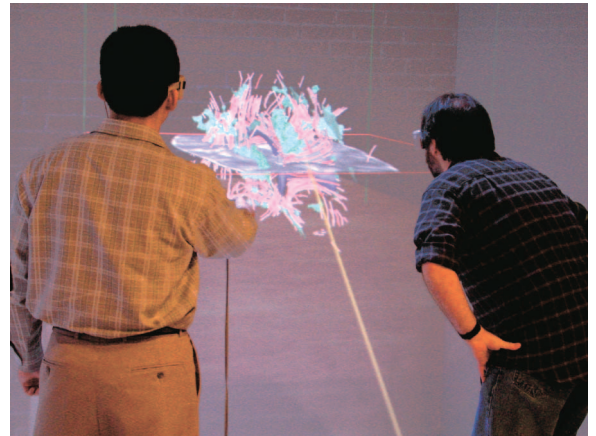


Fig. 9. The Cave's stereo display, large display surface, and interactivity help users understand the brain visualization.

T_2 -weighted MRI data, the position and orientation of which can be chosen interactively. We can also use the 2D section to carry any other data set that is registered with the 3D models. The user clicks a wand button to choose an axial, coronal, or sagittal section and uses two other buttons to move it back and forth. We also draw a yellow line akin to a laser pointer from the wand to where the wand is pointing (since physically pointing out an object is ineffective in the Cave).

For the environment, we texture-map the virtual walls and the floor in the same positions as the projection walls and floor and set up a table beneath the geometric models.

Fig. 9 shows two users interacting with the brain visualization in the Cave.

4 RESULTS AND DISCUSSION

We applied our method to a human brain data set with $256 \times 256 \times 40$ voxels and a resolution of $0.89\text{mm} \times 0.89\text{mm} \times 3.2\text{mm}$. Each slice of the data was acquired at a resolution of 128×128 and zero-filled. Figs. 10 and 11 show a visualization of the human brain on a desktop display (the indications of skull and eyes help orient the image). Through the semitransparent skull surface, we can see the ventricle (colored blue) in the middle and the streamtubes both around it and throughout the space.

The image shows that the streamtubes correlate well with major neural structures. The corpus callosum, depicted by the streamtubes running across the top of the ventricle, contains almost all the neurons that cross the brain from one hemisphere to the other. The internal capsule, clearly shown from the side view in Fig. 11, is the second most obvious white matter structure visible on a myelin stain and is the major fiber tract that carries information between the cortex and the brainstem. The cerebral peduncles are the continuation of the internal capsule as it runs down into the midbrain.

Several doctors and medical students who have used the system in the Cave found it easy to use. Users who have never used the Cave need a few minutes to become familiar with the system and the function of the wand buttons. Those who had also viewed images of the geometric models on a desktop screen reported that the 3D structures were

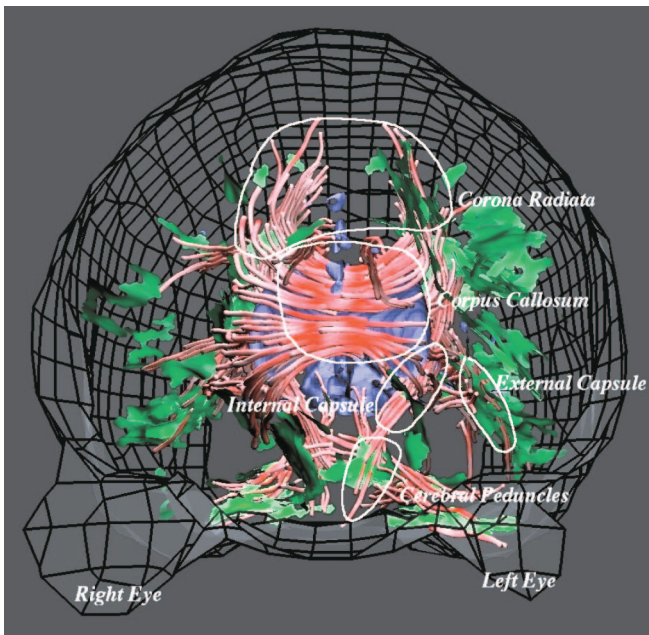


Fig. 10. Front view of the human brain data set visualization. The culling parameters are shown in Tables 1 and 2.

easier to understand in the virtual environment. The 2D sections were considered a very valuable tool. All our users were eager for more detail in the visualization, saying that more anatomical detail and streamtubes in the regions of interest would enhance their understanding. To this end, Fig. 12 shows the visualization of the same human brain data set used in Fig. 10 with the average linear anisotropy threshold set to 0.20: The number of streamtubes increases from 472 in Fig. 10 to 4,538 in Fig. 12. Setting more seed points will also increase the number of streamtubes. However, the level of detail we can visualize is fundamentally limited by the voxel size of the data set. Setting many seed points within one voxel will yield redundant streamtubes that will be discarded by the culling algorithm. We are also looking for methods that can switch smoothly between geometric models with different levels of detail.

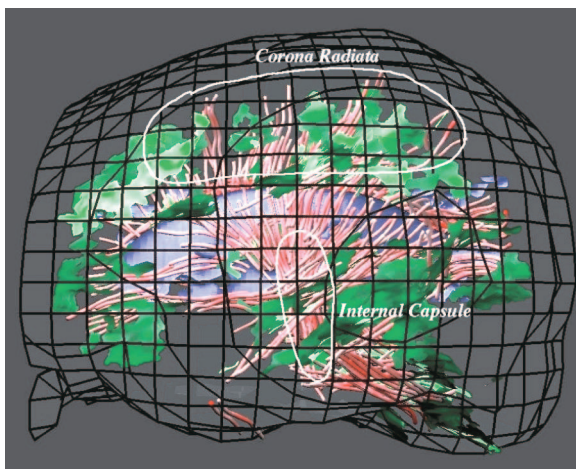


Fig. 11. Side view of the human brain data set visualization. The culling parameters are the same as those used in Fig. 10.

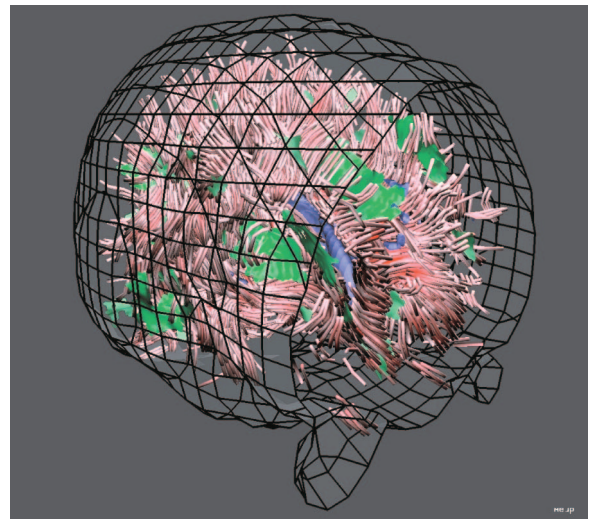


Fig. 12. Human brain data set visualization with average linear anisotropy threshold set to 0.20 instead of 0.30. The number of streamtubes increases from 472 to 4,538.

Users also made application-specific observations, discussed below.

4.1 Studying Changes in White-Matter Structures after Gamma-Knife Capsulotomy

One of the users, a doctor from Brown University-affiliated Butler Hospital, has been using DT-MRI data to study OCD patients, looking particularly at changes after radiation surgery that ablates an important white matter region. These changes should show up in the DT-MRI data, and the connectivity changes, which are inherently 3D, will be very difficult to see in sections alone. This work should help generate a number of specific hypotheses about the mechanism that makes this treatment modality successful. Patients are currently being identified to participate in the project.

4.2 Preoperative Brain Tumor Surgery Planning

We are working with two neurosurgeons from Massachusetts General Hospital on presurgical planning for tumor surgery. With the virtual environment, they believe that they can get a better spatial understanding of the critical anatomical structures in the vicinity of a targeted tumor, particularly white matter tracts. Their feedback suggests that 3D relationships between the tumor and other important structures, like vasculature and motor cortex, are useful information, and thus they would like to be able to display other scalar-valued images. For example, T1-weighted or contrast-agent-enhanced 2D sections could show the viable highly vascularized tumor regions. Together with other colleagues from MGH-Radiology, they are currently identifying surgical candidates from whom to collect MRI/DT-MRI for study in our virtual environment before surgery.

4.3 Further Discussion

Several issues in our methods warrant further discussion. First, we use thresholds to define regions of anisotropy. The thresholds lack a physiological basis, but nonetheless introduce an abrupt visual change between regions with diffusion values that are arbitrarily close. A model that

transitions smoothly within and among all three regimes, isotropic, planar, and linear, could avoid these abrupt changes.

A second issue is that the surface-generation algorithm assumes that the first two eigenvector fields define a locally Euclidean surface. This is true if and only if the Lie bracket of the major and medium eigenvector fields lies within the plane determined by the major and medium eigenvectors [3]. We have yet to test if the condition is satisfied by the first two eigenvector fields because calculating the Lie bracket is nontrivial. Significant errors are likely to be visually obvious; we have seen no such errors and also note that the features found are consistent with neural anatomy.

Third, the models our methods produce are sensitive to not only the information in the imaging data but also artifacts of the imaging process, including noise and averaging due to limited resolution. The averaging can hide the information from smaller features and create composite "features" that are not real. Noise can also perturb the models in inaccurate ways, particularly when coupled with the threshold effects described; a small amount of noise can cause a feature to disappear entirely or split into two smaller features. We avoid some of these problems by eliminating small features and regions of anisotropy likely to be solely due to noise. Expert feedback suggests that many of the features present in our models correlate well with known neural anatomy, but some artifacts certainly remain.

5 CONCLUSIONS

We have presented a new visualization method for second-order diffusion tensor fields acquired with DT-MRI. We separate different classes of anisotropy and map them to different visual icons: streamtubes and streamsurfaces. We generate a large set of visual icons and then select from them a representative subset for display. Anatomical landmarks and 2D sections showing T_2 -weighted MR images are also displayed to provide context. Display is on a traditional desktop computer and also within an immersive virtual reality application running in a Cave. These environments provide different advantages for interacting with the models and facilitate a better understanding of the anatomy and connectivity they represent.

Our experiments and feedback from several medical practitioners who used the models show that the streamtubes correlate well with major white-matter structures: The corpus callosum, internal capsule, and a number of other neural structures can be identified within the streamtubes. Users also report that the anatomical landmarks and 2D MR sections help them in exploring the data. The culling process is essential in reducing the overall number of geometric models while retaining a representative sample. Users have expressed interest in modifying the several user-defined thresholds involved in the generation and culling of the geometric models to select different subsets of the streamtubes and streamsurfaces for different purposes. Virtual reality has helped users understand the complex geometric models and several of our collaborative projects will continue to build on these models for specific biomedical applications.

ACKNOWLEDGMENTS

The authors thank Dr. Susumu Mori at Johns Hopkins University who kindly sent them the human brain data set. Thanks to Dan Morris and Charlie Curry for their help on ideas and coding. Thanks to Peter Basser and Carlo Pierpaoli for their suggestions. Thanks to Ben Greenberg, Thomas Deisboeck, Antonio Chiocca, David Berson, Eric Ahrens, Russell Jacobs, Seth Ruffins, and Rusty Lansford for providing feedback and evaluation of our results. Thanks to Andy Forsberg, Dan Keefe, and the Brown Graphics Group for their help with the Cave development and general discussions. Thanks to Morriah Horani, Brendan Kelleher, and Katrina Avery for reviewing this paper. This work was partially supported by the Human Brain Project (NIDA and NIMH), US National Institutes of Health (AR-44005), and US National Science Foundation (CCR-0086065, CCR-0093238, and EIA-9724347).

REFERENCES

- [1] P.J. Basser, J. Mattiello, and D. LeBihan, "Estimation of the Effective Self-Diffusion Tensor from the NMR Spin-Echo," *J. Magnetic Resonance B*, vol. 103, no. 3, pp. 247-254, Mar. 1994.
- [2] P.J. Basser, S. Pajevic, C. Pierpaoli, J. Duda, and A. Aldroubi, "In Vivo Fiber Tractography Using DT-MRI Data," *Magnetic Resonance in Medicine*, vol. 44, pp. 625-632, 2000.
- [3] R.L. Bishop and R.J. Crittenden, *Geometry of Manifolds*. Academic Press, 1964.
- [4] J. Cormans, R. Luypaert, F. Verhelle, T. Stadnik, and M. Osteaux, "A Method for Myelin Fiber Orientation Mapping Using Diffusion-Weighted MR Images," *Magnetic Resonance Imaging*, vol. 44, pp. 443-454, 1994.
- [5] C. Cruz-Neira, D.J. Sandin, and T.A. DeFanti, "Surround-Screen Projection-Based Virtual Reality: The Design and Implementation of the CAVE," *Computer Graphics (SIGGRAPH '93 Proc.)*, J.T. Kajiya, ed., vol. 27, pp. 135-142, Aug. 1993.
- [6] T. Delmarcelle and L. Hesselink, "Visualizing Second-Order Tensor Fields with Hyperstream Lines," *IEEE Computer Graphics and Applications*, vol. 13, no. 4, pp. 25-33, July 1993.
- [7] D.F. Scollan, A. Holmes, R. Winslow, and J. Forder, "Histological Validation of Myocardial Microstructure Obtained from Diffusion Tensor Magnetic Resonance Imaging," *Am. J. Physiology*, vol. 275, pp. H2308-2318, 1998.
- [8] M.A.Z. Dippé and E.H. Wold, "Antialiasing through Stochastic Sampling," *Computer Graphics (SIGGRAPH '85 Proc.)*, B.A. Barsky, ed., vol. 19, pp. 69-78, July 1985.
- [9] E.W. Hsu, A.L. Muzikant, S.A. Matulevicius, R.C. Penland, and C.S. Henriquez, "Magnetic Resonance Myocardial Fiber-Oriented Mapping with Direct Histological Correlation," *Am. J. Physiology*, vol. 274, pp. H1627-1634, 1998.
- [10] J. V. Hajnal, M. Doran, A.S. Hall, A.G. Collins, A. Oatridge, J.M. Pennock, I.R. Young, and G.M. Bydder, "MR Imaging of Anisotropically Restricted Diffusion of Water in the Nervous System: Technical, Anatomic and Pathologic Considerations," *J. Computer Assisted Tomography*, vol. 15, pp. 1-18, 1991.
- [11] G.L. Kindlmann and D.M. Weinstein, "Hue-Balls and Lit-Tensors for Direct Volume Rendering of Diffusion Tensor Fields," *Proc. IEEE Visualization '99*, pp. 183-190, 1999.
- [12] D.H. Laidlaw, E.T. Ahrens, D. Kremers, M.J. Avalos, C. Readhead, and R.E. Jacobs, "Visualizing Diffusion Tensor Images of the Mouse Spinal Cord," *Proc. Visualization '98*, 1998.
- [13] L.R. Frank, "Anisotropy in High Angular Resolution Diffusion-Weighted MRI," *Magnetic Resonance in Medicine*, vol. 45, pp. 935-939, 2001.
- [14] M.E. Moseley, J. Kuckarczyk, H.S. Asgari, and D. Norman, "Anisotropy of Diffusion-Weighted MRI," *Magnetic Resonance in Medicine*, vol. 19, pp. 321-326, 1991.
- [15] S. Mori, B.J. Crain, V.P. Chacko, and P.C.M. van Zijl, "Three Dimensional Tracking of Axonal Projections in the Brain by Magnetic Resonance Imaging," *Ann. Neurology*, vol. 45, pp. 265-269, 1999.

- [16] C. Pierpaoli and P.J. Basser, "Toward a Quantitative Assessment of Diffusion Anisotropy," *Magnetic Resonance in Medicine*, vol. 36, pp. 893-906, 1996.
- [17] W.H. Press, S.A. Teukolsky, W.T. Vetterling, and B.P. Flannery, *Numerical Recipes in C: The Art of Scientific Computing*, second ed. New York: Cambridge Univ. Press, 1992.
- [18] R.R. Dickinson, "A Unified Approach to the Design of Visualization Software for the Analysis of Field Problems," *Three-Dimensional Visualization and Display Technologies (Proc. SPIE)*, pp. 173-180, 1989.
- [19] C. Upson, T. Faulhaber Jr., D. Kamins, D. Laidlaw, D. Schlegel, J. Vroom, R. Gurwitz, and A. van Dam, "The Application Visualization System: A Computational Environment for Scientific Visualization," *IEEE Computer Graphics and Applications*, vol. 9, no. 4, pp. 30-42, July/Aug. 1989.
- [20] D.M. Weinstein, G.L. Kindlmann, and E.C. Lundberg, "Tensor-lines: Advection-Diffusion Based Propagation through Diffusion Tensor Fields," *Proc. IEEE Visualization '99*, pp. 249-254, 1999.
- [21] C.F. Westin, S.E. Maier, B. Khidhir, P. Everett, F.A. Jolesz, and R. Kikinis, "Image Processing for Diffusion Tensor Magnetic Resonance Imaging," *Proc. Int'l Conf. Medical Image Computing and Computer-Assisted Intervention (MICCAI '99)*, pp. 441-452, 1999.
- [22] C.F. Westin, S. Peled, H. Gubjartsson, R. Kikinis, and F.A. Jolesz, "Geometrical Diffusion Measures for MRI from Tensor Basis Analysis," *Proc. Int'l Soc. Magnetic Resonance in Medicine (ISMRM)*, 1997.
- [23] R. Xue, P.C.M. van Zijl, B.J. Crain, M. Solaiyappan, and S. Mori, "In Vivo Three-Dimensional Reconstruction of Rat Brain Axonal Projections by Diffusion Tensor Imaging," *Magnetic Resonance in Medicine*, vol. 42, pp. 1123-1127, 1999.
- [24] S. Zhang, Ç. Demiralp, D. Keefe, M. DaSilva, B.D. Greenberg, P.J. Basser, C. Pierpaoli, E.A. Chiocca, T.S. Deisboeck, and D. Laidlaw, "An Immersive Virtual Environment for DT-MRI Volume Visualization Applications: A Case Study," *Proc. IEEE Visualization '01*, pp. 437-440, Oct. 2001.
- [25] S. Zhang and D. Laidlaw, "Elucidating Neural Structure in Diffusion Tensor MRI Volumes Using Streamtubes and Stream-surfaces," *Proc. Int'l Soc. Magnetic Resonance in Medicine (ISMRM)*, 2001.
- [26] S. Zhang, D.H. Laidlaw, Ç. Demiralp, M. DaSilva, D.F. Keefe, B.D. Greenberg, P.J. Basser, C. Pierpaoli, E.A. Chiocca, and T.S. Deisboeck, "Toward Application of Virtual Reality to Visualization of DT-MRI Volumes," *Proc. Int'l Conf. Medical Image Computing and Computer-Assisted Intervention (MICCAI '01)*, Oct. 2001.



Song Zhang received the BS degree in computer science from Nankai University, China, in 1996. He worked on optical character recognition algorithms in the Nankai Institute of Machine Intelligence from 1996 to 1998. Since 1998, he has been a computer science doctoral student at Brown University, Providence, Rhode Island. His research interests include scientific visualization, medical imaging techniques, and computer graphics.



Çagatay Demiralp received the BS degree in computer science from Ege University, Izmir, Turkey, in 2000. He is currently a master's student in computer science at Brown University, Providence, Rhode Island.



David Laidlaw received the PhD degree in computer science from the California Institute of Technology, where he also did postdoctoral work in the Division of Biology. He is an assistant professor of computer science at Brown University, Providence, Rhode Island. His research centers applying concepts from visualization, modeling, computer graphics, and computer science to other scientific disciplines.

► For more information on this or any computing topic, please visit our Digital Library at <http://computer.org/publications/dlib>.